

Article

Study of CHF₃/CH₂F₂ Adsorption Separation in TIFSIX-2-Cu-i

 Shoudong Wang¹, Lei Zhou², Hongyun Qin¹, Zixu Dong¹, Haoyuan Li¹, Bo Liu¹, Zhilu Wang¹, Lina Zhang¹, Qiang Fu^{1,*}  and Xia Chen^{1,*}

¹ School of Chemistry and Chemical Engineering, Shandong University of Technology, Zibo 255049, China; jokemaker_wxs@163.com (S.W.); hongyunqin@163.com (H.Q.); qilin199823@sina.com (Z.D.); lhy_1999@foxmail.com (H.L.); liubo1245935971@163.com (B.L.); sevenwangzl@163.com (Z.W.); zln20000521@163.com (L.Z.)

² Shandong Dongyue Organosilicon Materials Co., Ltd., Zibo 256401, China; zhoulei@dyyjg.com

* Correspondence: fuqiang@tju.edu.cn (Q.F.); hgxychx@sdut.edu.cn (X.C.)

Abstract: Hydrofluorocarbons (HFCs) have important applications in different industries; however, they are environmentally unfriendly due to their high global warming potential (GWP). Hence, reclamation of used hydrofluorocarbons via energy-efficient adsorption-based separation will greatly contribute to reducing their impact on the environment. In particular, the separation of azeotropic refrigerants remains challenging, such as typical mixtures of CH₂F₂ (HFC-23) and CHF₃ (HFC-32), due to a lack of adsorptive mechanisms. Metal–organic frameworks (MOFs) can provide a promising solution for the separation of CHF₃–CH₂F₂ mixtures. In this study, the adsorption mechanism of CHF₃–CH₂F₂ mixtures in TIFSIX-2-Cu-i was revealed at the microscopic level by combining static pure-component adsorption experiments, molecular simulations, and density-functional theory (DFT) calculations. The adsorption separation selectivity of CH₂F₂/CHF₃ in TIFSIX-2-Cu-i is 3.17 at 3 bar under 308 K. The existence of similar TiF₆²⁻ binding sites for CH₂F₂ or CHF₃ was revealed in TIFSIX-2-Cu-i. Interactions between the fluorine atom of the framework and the hydrogen atom of the guest molecule were found to be responsible for determining the high adsorption separation selectivity of CH₂F₂/CHF₃. This exploration is important for the design of highly selective adsorbents for the separation of azeotropic refrigerants.

Keywords: adsorption mechanism; CHF₃/CH₂F₂ adsorptive separation; adsorption site; adsorption heat; TIFSIX-2-Cu-i



Citation: Wang, S.; Zhou, L.; Qin, H.; Dong, Z.; Li, H.; Liu, B.; Wang, Z.; Zhang, L.; Fu, Q.; Chen, X. Study of CHF₃/CH₂F₂ Adsorption Separation in TIFSIX-2-Cu-i. *Molecules* **2024**, *29*, 1721. <https://doi.org/10.3390/molecules29081721>

Academic Editor: Michel Dumon

Received: 2 March 2024

Revised: 3 April 2024

Accepted: 9 April 2024

Published: 11 April 2024



Copyright: © 2024 by the authors. Licensee MDPI, Basel, Switzerland. This article is an open access article distributed under the terms and conditions of the Creative Commons Attribution (CC BY) license (<https://creativecommons.org/licenses/by/4.0/>).

1. Introduction

HFCs are third-generation fluorinated gases (F-gases), a class of synthetic compounds used primarily in refrigeration and air conditioning (RAC) [1–3]. HFCs are potent greenhouse gases. So, their production and application must be phased down to meet the emission reduction target according to the Montreal Protocol [4,5]. Depending on the actual production and use of refrigerants, many of the HFCs currently in use are azeotropic or near-azeotropic refrigerant mixtures [6]. The current mainstream refrigerants include R-444A, R-447A, and R-448A, which are blends of HFCs (R-32, R-125, R-23, R-134a, etc.) with hydrofluoroolefins (HFOs). Difluoromethane (CH₂F₂, GWP = 675) and trifluoromethane (CHF₃, GWP = 14,800) are the most common components of refrigerant mixture currently used in the refrigeration and air conditioning industry, with very high GWP [7,8]. Therefore, to control HFC emissions, the first thing is to separate the components from the mixtures efficiently. However, due to the low efficiency of cryogenic distillation to separate refrigerant mixtures, the amount of refrigerant gas recovered remains low. There are very similar physical properties and molecular dynamics diameters for CHF₃/CH₂F₂ molecules, which makes the search for alternative technologies to energy-intensive distillation processes very challenging. In this study, CHF₃/CH₂F₂ was chosen as a sample to study the separation mechanism to provide a reference for

the subsequent separation of HFCs. Selective adsorption technology has become an attractive solution for gas separation considering energy efficiency and environmental protection [9–12]. Metal–organic framework (MOF) materials show great promise for gas storage and separation applications due to their significant advantages, such as flexible framework, tunable pore size and structure, and ultra-high specific surface area [13–19].

However, the practical applications of some MOFs are limited by their poor structural stability due to strong dependence on solvent molecules. The framework structure will collapse if they are exposed to air, high-strength acids, and bases for a period of time. TIFSIX-2-Cu-i is easy to regenerate and thermally stable under air atmosphere [20,21]. The efficient separation of C₂H₂/C₂H₄ by TIFSIX-2-M-i has been demonstrated by previous studies [20,22,23]. Inspired by these findings, TIFSIX-2-Cu-i was chosen to study the separation of CHF₃–CH₂F₂ mixtures. To our knowledge, previous work on the mechanism of CHF₃/CH₂F₂ adsorption in TIFSIX-2-Cu-i is sparse, which is disadvantageous to understanding and predicting interactions between adsorbates and adsorbents. In this study, the feasibility of selective separation of CHF₃/CH₂F₂ by TIFSIX-2-Cu-i was evaluated for the first time. The method of adding polarization to a generic forcefield was used to obtain simulated and experimentally consistent adsorption isotherms, ensuring the accuracy of the forcefield. In this work, TIFSIX-2-Cu-i exhibits preferential adsorption of CH₂F₂ over CHF₃ with a high CH₂F₂ adsorption capacity (2.70 mmol/g at 298 K and 1 bar). Thermodynamic and kinetic analyses were carried out by a combination of adsorption experiments and molecular simulations. The adsorption selectivity, isosteric adsorption heat, and binding sites were investigated. In addition, these works are of great significance for exploring the adsorption separation of HFCs by fluorinated anion MOFs.

2. Results and Discussion

2.1. Adsorption Isotherm

To verify the accuracy of the forcefield, the present work compares the simulation adsorption isotherms for pure CHF₃ or CH₂F₂ in TIFSIX-2-Cu-i at 288, 298, and 308 K with experimental adsorption isotherms (Figure 1). The simulation results under pressure values from 0 bar to 3 bar are in good agreement with the experimental data. Therefore, it can be inferred that the potential model and polarization forcefield parameters used are reliable for predicting the adsorption of CHF₃ and CH₂F₂. For all three temperatures, the trends of the CHF₃ and CH₂F₂ isotherms are similar. These adsorption isotherms were fitted with the Langmuir isotherm model. The Langmuir equation is defined as shown in Equation (1). The parameters of the isotherms for CHF₃ and CH₂F₂ are summarized in Table 1.

$$q_e = q_m b p / (1 + b p) \quad (1)$$

where q_e is the equilibrium adsorption capacity, q_m is the maximum adsorption capacity, b is the adsorbate–adsorbent affinity coefficient, and p is the equilibrium pressure. From Table 1, parameter b decreases with increasing temperature at the same adsorbate; parameter b is consistently larger for CH₂F₂ than for CHF₃ at all three temperatures. The interaction of CH₂F₂ with the framework was stronger compared to CHF₃. Parameter q_m shows a larger maximum adsorption capacity for CH₂F₂.

Table 1. Parameters of CHF₃ and CH₂F₂ fitted by the Langmuir Adsorption Isotherm Model.

	T (K)	q_m (mmol/g)	b (bar ^{−1})	R-Squared
CH ₂ F ₂	288	6.22417	0.85526	0.9582
	298	7.06367	0.57236	0.97048
	308	6.97756	0.44233	0.9712
CHF ₃	288	4.92555	0.51897	0.976526
	298	4.22734	0.47127	0.96737
	308	3.8638	0.38144	0.9911

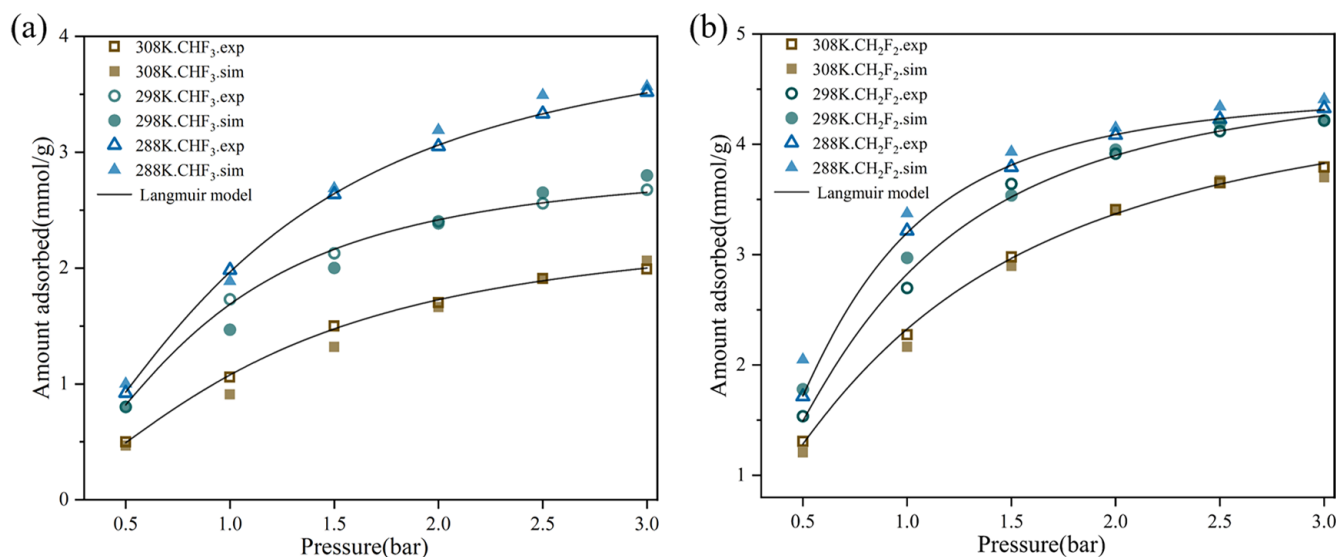


Figure 1. The experimental and simulated adsorption isotherms for pure CHF₃ (a) or CH₂F₂ (b) at 288, 298, and 308 K in TIFSIX-2-Cu-i.

In detail, the uptake of CHF₃ and CH₂F₂ reached 1.73 and 2.70 mmol/g at 1 bar and 298 K, respectively. At 308 K and 3 bar, the uptake of CH₂F₂ was 3.79 mmol/g, which is almost double the CHF₃ uptake (1.99 mmol/g). At the same temperature and pressure, the adsorption capacity of CH₂F₂ was higher than that of CHF₃. Thus, there was a greater adsorption affinity for CH₂F₂ than CHF₃. The adsorption capacity of both CHF₃ and CH₂F₂ increased significantly with increasing pressure. However, the adsorption capacity of CH₂F₂ increased faster compared to that of CHF₃. These findings suggest that TIFSIX-2-Cu-i has stronger binding ability regarding CH₂F₂, indicating that TIFSIX-2-Cu-i is a potential material to separate CHF₃/CH₂F₂ mixtures with high efficiency.

2.2. Adsorption Selectivity and Heat

In this section, thermodynamic adsorption selectivity and isosteric adsorption heat were explored, which were calculated from experimental measurements. In addition, molecular dynamics simulations were performed to explore the diffusivity of guest molecules in TIFSIX-2-Cu-i.

Myers and Praunitz developed ideal adsorbed solution theory (IAST). Here, the multicomponent adsorption equilibrium of CHF₃ or CH₂F₂ was predicted using ideal adsorbed solution theory (IAST), which was calculated by the following equation [24]:

$$S = (x_1/x_2)/(y_1/y_2) \quad (2)$$

where S is the selectivity of a component versus another one (e.g., CH₂F₂/CHF₃), x is the molar fraction in the adsorbed phase, and y is the molar fraction in the gas phase. The relatively high adsorption separation selectivity is shown in Figure 2. The selectivity of CH₂F₂/CHF₃ is greater than 1.0 at all the adsorption isotherms, indicating that TIFSIX-2-Cu-i preferentially adsorbs CH₂F₂. At 298 K and 308 K, selectivity increases with increasing pressure, while, at 288 K, selectivity decreases slightly with increasing pressure. At 288 K, the adsorption amount of CH₂F₂ in the high-pressure zone flattens more as pressure rises compared to CHF₃. We hypothesize that most of the adsorption sites of the framework were then occupied by CH₂F₂ molecules, making it difficult for the newly added CH₂F₂ molecules to find available adsorption sites, leading to slowdown of the adsorption rate.

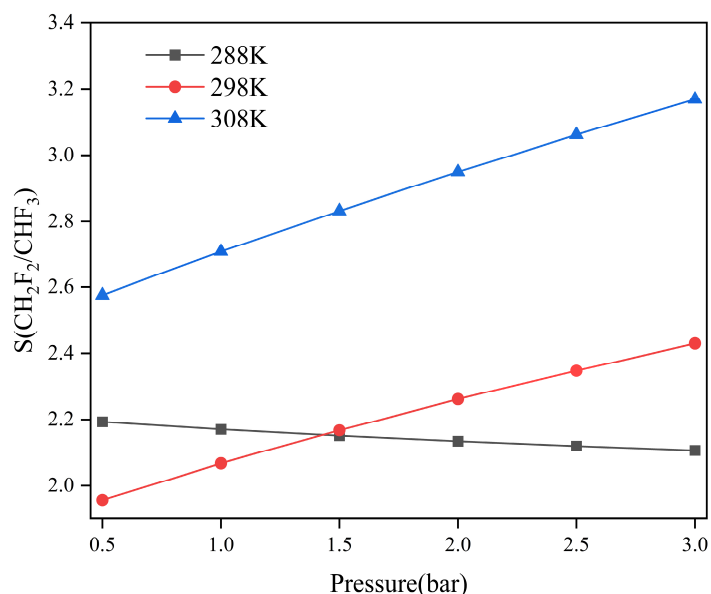


Figure 2. The adsorption separation selectivity for CH₂F₂ over CHF₃ in TIFSIX-2-Cu-i at different temperatures and pressures, which correspond to the CH₂F₂-CHF₃ mixture (CH₂F₂/CHF₃, 50/50, v/v).

To assess the interaction strength between the framework and gas molecules, we utilized single-component isotherms obtained at three distinct temperatures (Figure 1) to determine the isosteric adsorption heat (Q_{st}) of CH₂F₂/CHF₃ on TIFSIX-2-Cu-i. The isosteric adsorption heat was calculated indirectly using the Clausius–Clapeyron equation [25]:

$$\frac{d \ln P}{dT} = \frac{q_i}{RT} \quad (3)$$

where q_i refers to the isosteric heat of adsorption, kJ/mol; P is the pressure, MPa; T is the temperature, K; and R is the gas constant, 8.314 J/(mol·K). As shown in Figure 3, the Q_{st} values of CHF₃ and CH₂F₂ were around 20 and 23 kJ/mol^{−1}. The heat of adsorption of CH₂F₂ was always higher than the heat of adsorption of CHF₃ in TIFSIX-2-Cu-i. Therefore, it is directly verified that TIFSIX-2-Cu-i interacts more strongly with CH₂F₂ than CHF₃, which leads to greater adsorption of CH₂F₂ than CHF₃.

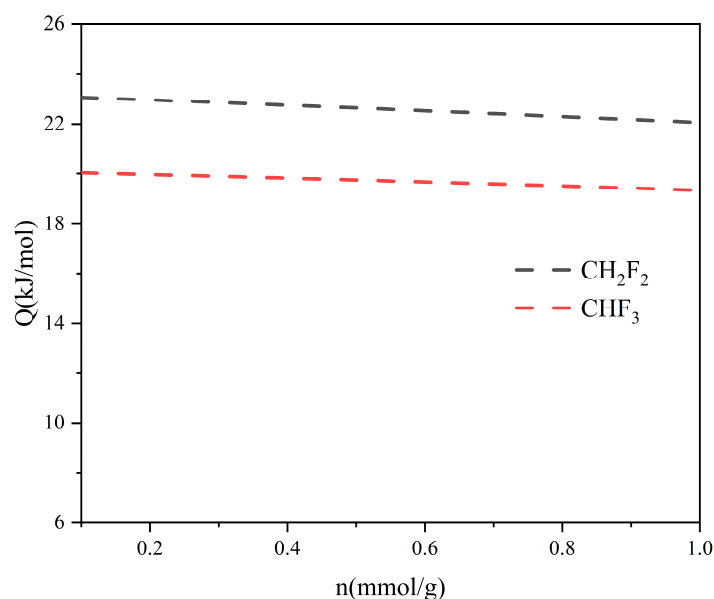


Figure 3. The isosteric adsorption heat (Q_{st}) of CH₂F₂/CHF₃ on the TIFSIX-2-Cu-i.

In this part, the free diffusion behavior of CHF_3 and CH_2F_2 in TIFSIX-2-Cu-i was explored. The corresponding mean square displacements (MSDs) obtained from the simulations are shown in Figure 4. The self-diffusion coefficients of CHF_3 and CH_2F_2 in the TIFSIX-2-Cu-i were calculated using the Einstein relation as shown below:

$$D = \frac{1}{6} \lim_{n \rightarrow \infty} \frac{d}{dt} \left\{ \frac{1}{N_i} \sum_{i=1}^{N_i} \langle |r_i(t) - r_i(0)|^2 \rangle \right\} \quad (4)$$

where the average is taken over time t for the mean square displacement of the center of mass position vectors r of all the molecules N in the system; $\langle \rangle$ indicates the overall average. The calculated results show that the self-diffusion coefficients of CHF_3 and CH_2F_2 are $1.15 \times 10^{-4} \text{ cm}^2/\text{s}$ and $2.18 \times 10^{-4} \text{ cm}^2/\text{s}$, respectively. This finding showed that TIFSIX-2-Cu-i exhibited high kinetic selectivity for CH_2F_2 over CHF_3 . TIFSIX-2-Cu-i is a doubly interpenetrated framework attributed to the much longer organic linker 4,4-dipyridylacetylene and slightly large pore sizes of about $5.2 \times 5.2 \text{ \AA}$. That makes it easier for the mixture to diffuse into the adsorption sites within the pores. The properties of this MOF can be characterized as pillared square lattice networks with a pcu topology, attributed to their pore surfaces with narrow pore sizes and highly electrostatic pore surfaces. These features combined provide exceptionally strong binding interactions with polarizable molecules, such as CHF_3 and CH_2F_2 [26]. This also enabled the two guest molecules to possess high adsorption capacity.

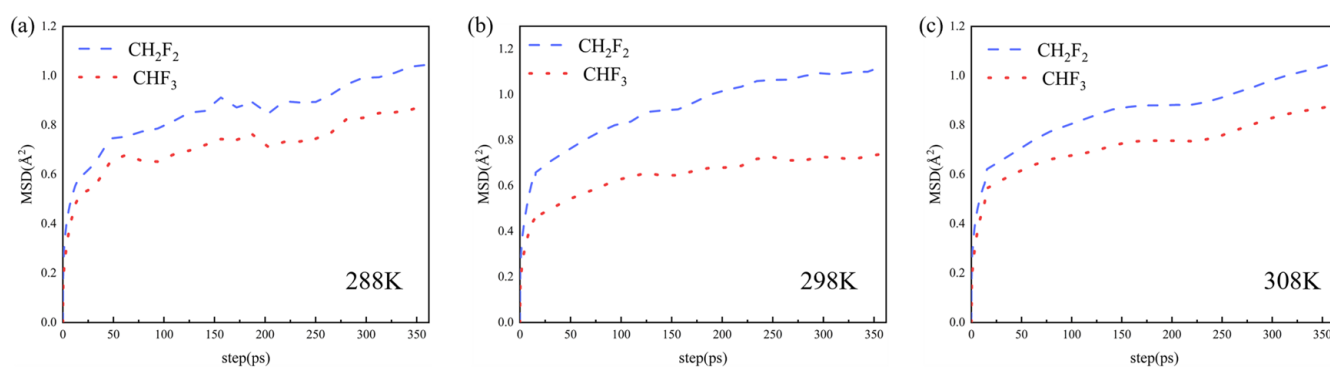


Figure 4. Mean-square displacements for CHF_3 – CH_2F_2 mixture ($\text{CHF}_3/\text{CH}_2\text{F}_2$, 50/50, v/v) in TIFSIX-2-Cu-i at 288 K (a), 298 K (b), and 308 K (c).

2.3. Adsorption Sites

Figure 5 shows the optimal adsorption binding sites for CHF_3 and CH_2F_2 . The snapshots obtained detailed information about the adsorption of pure CHF_3 and CH_2F_2 in TIFSIX-2-Cu-i at 298 K and 1 bar. In the doubly interpenetrated framework of TIFSIX-2-Cu-i, the H atom of CHF_3 binds with the F atom from TiF_6^{2-} . The distance of the C–H...F hydrogen bond was 2.372 Å (Figure 5b). The distance of the C–H...F hydrogen bond was 2.372 Å obtained by the simulation was smaller than the sum of the van der Waals radii of H and F (2.55 Å) [27], confirming the existence of electrostatic interactions for $\text{H}^{\delta+} \cdots \text{F}^{\delta-}$. This was consistent with the reported binding sites of TIFSIX-2-Cu-i to short-chain alkanes (C_2H_2 , C_2H_4) [20,22,23]. CH_2F_2 has a similar binding site. The two H atoms of CH_2F_2 are bound at the F site by virtue of a synergistic hydrogen bonding interaction. The shortest length of the C–H...F bond between CH_2F_2 and the TiF_6^{2-} site is 2.172 Å, which is shorter than the C–H...F between CHF_3 and TiF_6^{2-} . The TIFSIX-2-Cu-i interacts more strongly with CH_2F_2 than CHF_3 .

Radial Distribution Functions (RDFs) amount to one of the most common methods for determination of interatomic distances. The RDFs in 298 K describing the interactions between the individual atoms of the pure $\text{CHF}_3/\text{CH}_2\text{F}_2$ and the TIFSIX-2-Cu-i framework are shown in Figure 6a,b. In Figure 6a, the framework interacts preferentially with H in CHF_3 . From the investigation of the RDF of H (CHF_3) with each atom of the framework in

Figure 6c, it was found that F (framework) interacts preferentially with H (CHF_3), which is the same as the snapshot conclusion of Figure 5a. Similarly, according to Figure 6b,d, it is found that F (framework) interacts preferentially with H (CH_2F_2). Compared to CHF_3 , CH_2F_2 has more H–F bonds interacting with the framework at the same time. So, we believe that the reason for the higher adsorption affinity of CH_2F_2 than CHF_3 is due to the binding geometry of $\text{CH}_2\text{F}_2/\text{CHF}_3$ adsorbed in the supercage of TIFSIX-2-Cu-i.

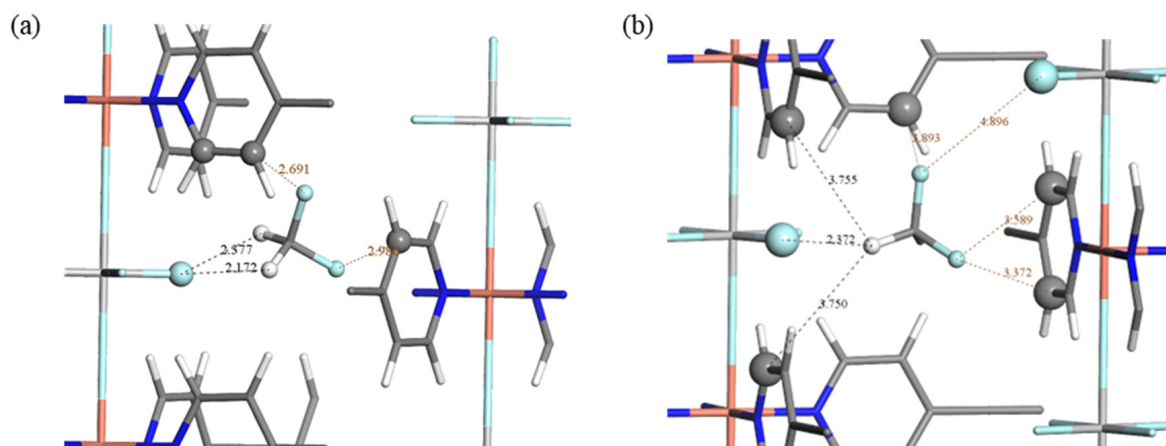


Figure 5. The typical binding sites for CH_2F_2 (a) or CHF_3 (b) in TIFSIX-2-Cu-i. The cyan, gray, and white spheres represent fluorine, carbon, and hydrogen atoms, respectively.

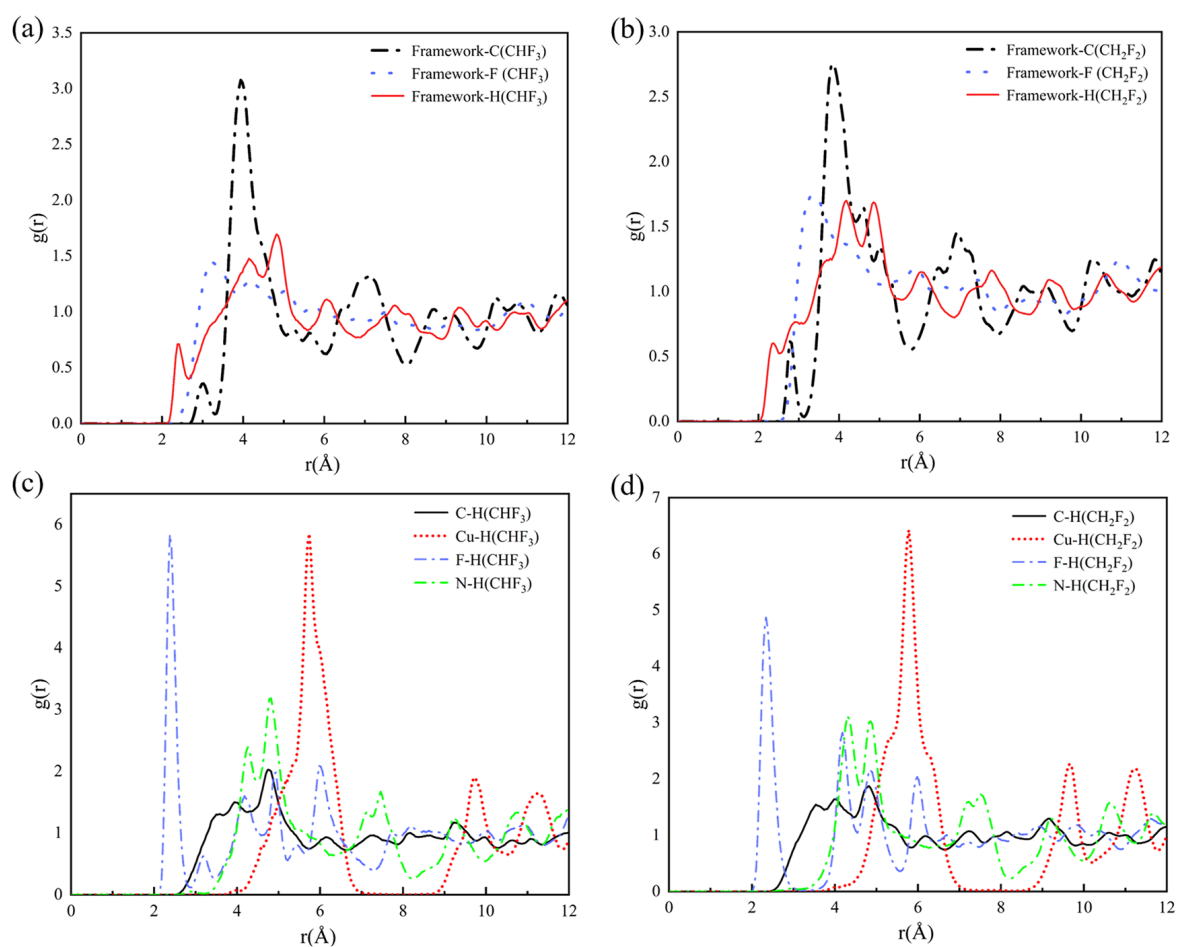


Figure 6. The RDF between the framework and each atom of CHF_3 (a)/ CH_2F_2 (b); the RDF between the representative atoms on the framework and hydrogen atom of CHF_3 (c)/ CH_2F_2 (d) in 298 K.

2.4. Redistribution of Charge Density

In order to study the charge change in TIFSIX-2-Cu-i after adsorption, DFT calculations were carried out to investigate the redistribution of charge density in this system after adsorption of $\text{CHF}_3/\text{CH}_2\text{F}_2$ molecules. As shown in Figure 7, the electrons of the H atoms of $\text{CHF}_3/\text{CH}_2\text{F}_2$ migrate to the F atoms of the framework due to the strong electron-withdrawing ability of the F atoms, where “-” denotes a negative charge. As shown in Figure 8, the blue area in Figure 8b is larger and darker than in Figure 8a, and the charge density transfer between CH_2F_2 and the framework F atom is more pronounced. This may be because, compared to CHF_3 , CH_2F_2 has more interactions between H atoms and framework F atoms, which is also the reason for the relatively high adsorption selectivity for CH_2F_2 over CHF_3 .

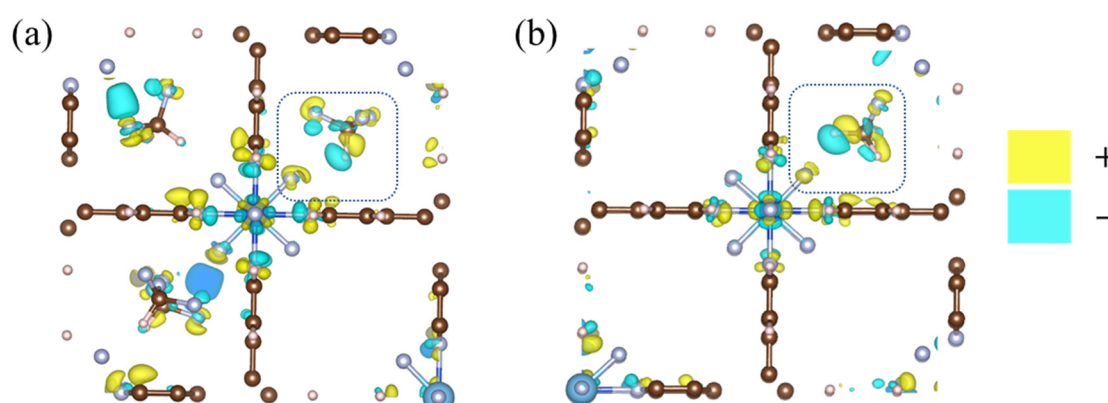


Figure 7. The redistribution of charge density in TIFSIX-2-Cu-i after adsorbing CHF_3 molecules (a) or CH_2F_2 molecules (b). Color code: brown, C; meat pink, H; silver, F; blue, Ti.

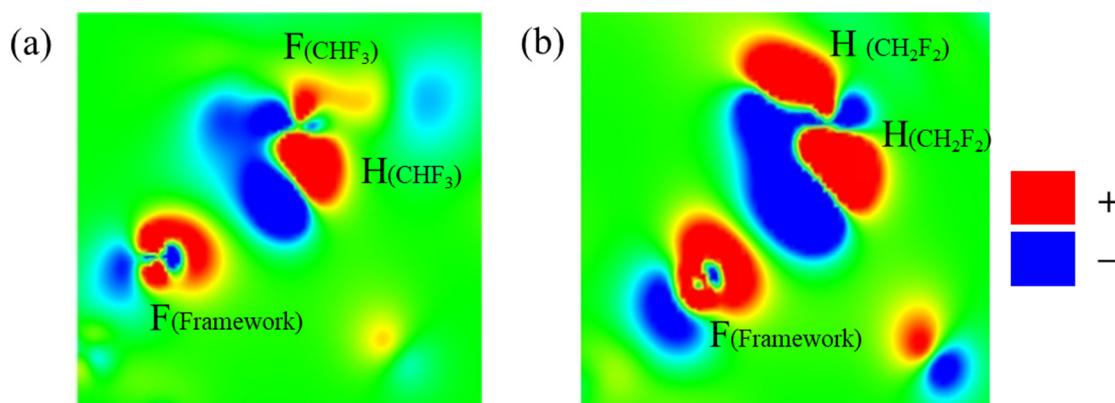


Figure 8. The slices of charge density redistribution for TIFSIX-2-Cu-i and CHF_3 (a)/ CH_2F_2 (b) after molecular adsorption, which correspond to the electron transfer between hydrogen atom of $\text{CHF}_3/\text{CH}_2\text{F}_2$ and the fluorine atom of TIF_6^{2-} .

3. Experiment Section

3.1. Preparation of Materials

All reagents and solvents were obtained commercially and used as received without further purification. Copper fluoroborate [$\text{Cu}(\text{BF}_4)_2$, 98.5%], methanol (CH_3OH , 99%), and ammonium hexafluoro titanate ($(\text{NH}_4)_2\text{TiF}_6$, 98%) were bought from Aladdin; 1,2-Di(pyridin-4yl)ethyne ($\text{C}_{12}\text{H}_8\text{N}_2$, 99.35%) was purchased from Leyan Co., Ltd. (Shanghai, China); and helium (He , 99.999%) gas was purchased from BaiYan Co., Ltd. (Zibo, China); The methylene fluoride (CH_2F_2 , 99.999%) and the methyl trifluoride (CHF_3 , 99.999%) were obtained from Dong Yue Co., Ltd. (Zibo, China).

3.2. Synthetic Procedures

$\text{Cu}(\text{BF}_4)_2$ (1 mmol), $(\text{NH}_4)_2\text{TiF}_6$ (1 mmol), and 1,2-Di(pyridin-4yl) ethyne (2 mmol) were dissolved in 5 mL of water and 10 mL of methanol, and a blue slurry product was obtained after stirring at 338 K for 12 h. Then, the slurry was filtered and washed with 10 mL of methanol. The blue filter cake was heated at 393 K for 12 h under vacuum conditions to obtain TIFSIX-2-Cu-i material [26].

3.3. Characterization

The activated TIFSIX-2-Cu-i was subjected to X-ray diffraction characterization and scanned using a Bruker AXS D8 ADVANCE diffractometer under a $\text{CuK}\alpha$ radiation source operated at a voltage of 40 kV, a current of 20 mA, and a scattering angle in the range (2θ) of 5–40 degrees. The XRD pattern of TIFSIX-2-Cu-i was presented in Figure 9, which was compared to calculated patterns. ASAP 2460 (Micromeritics company, Shanghai, China) was employed in this experiment. Pore structure was characterized by the N_2 adsorption method. The experimental temperature was 77 K. Before testing, the sample was treated by 12 h vacuumization at 393 K. Specific surface area was calculated using a multipoint Brunauer–Emmett–Teller model (BET). Table 2 shows the pore parameters of TIFSIX-2-Cu-i.

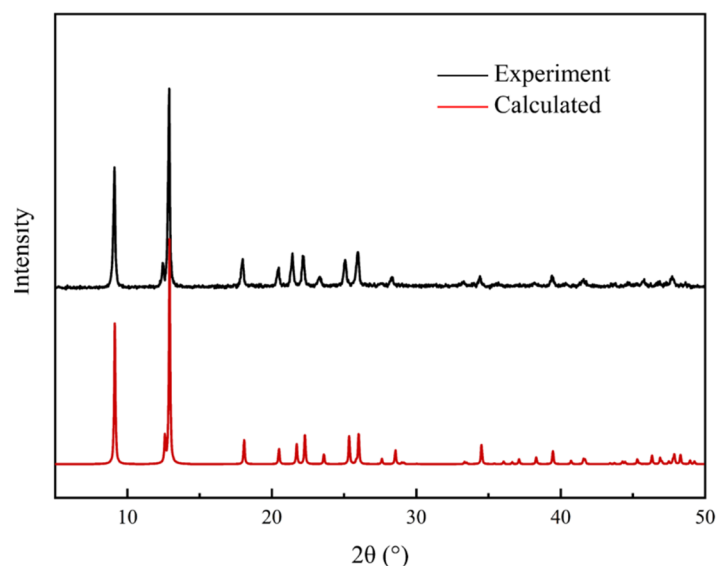


Figure 9. XRD patterns of TIFSIX-2-Cu-i after activation (compared to calculated patterns).

Table 2. Pore parameters of TIFSIX-2-Cu-i.

S_{BET} (m^2/g)	Sample Density (cm^3/g)	Total Pore Volume (cm^3/g)	t-Plot Micropore Volume (cm^3/g)	Mesopore Volume (cm^3/g)	Average Pore Size (Å)
372	1.211	0.211	0.131	0.079	3.988

3.4. Single-Component Adsorption Measurements

The adsorption isotherms of CHF_3 and CH_2F_2 were measured in the absolute pressure range of 1–3 bar in TIFSIX-2-Cu-i framework. The experimental temperatures were 288, 298, and 308 K. Excess adsorption experiments were performed using activated TIFSIX-2-Cu-i monomer. The temperature was controlled by an external circulating water bath. Before the measurements, TIFSIX-2-Cu-i was degassed at 393 K for 12 h under vacuum conditions. CHF_3 and CH_2F_2 gas of purity 99.99% were used as adsorbates. The adsorption capacity of pure CHF_3 or CH_2F_2 was calculated based on the pressure changes before and after adsorption. Figure 10 shows the diagram of adsorption measurements' experimental apparatus. A standard volumetric method was used to measure pure gas adsorption isotherms [28]. The homemade apparatus is designed by the proposed method.

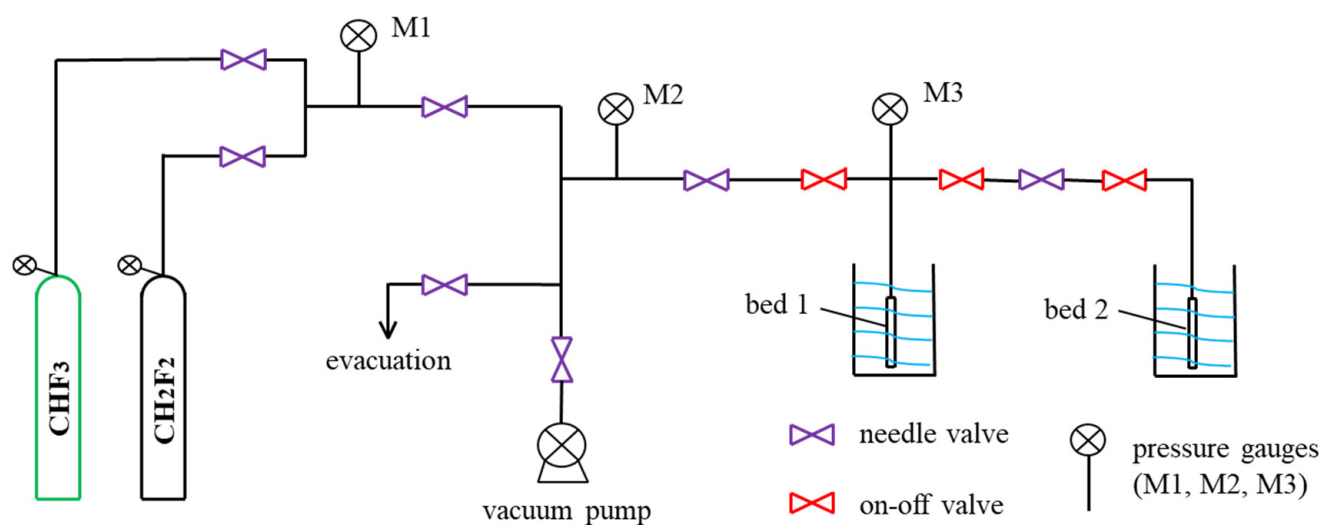


Figure 10. Diagram of adsorption measurements' experimental apparatus.

4. Models and Methods

4.1. Models

The interpenetrated polymorph, TIFSIX-2-Cu-i, is composed of doubly interpenetrated nets that are isostructural to the nets in TIFSIX-2-Cu. The independent nets are staggered with respect to one another, affording 5.2 Å pores [22,23]. The crystal cells used in the simulation were downloaded from the Cambridge Crystallographic Data Center (CCDC) as structural files. Optimized structure by DFT simulation was used for further calculations. TIFSIX-2-Cu-i is a variant of SIFSIX-2-Cu-i. Ti⁴⁺ has a higher polarizability relative to Si⁴⁺ [29]. So, TIFSIX-2-Cu-i has a higher thermal stability (decomposition temperature of 262 °C), which may be attributed to the relatively higher polarizability of Ti⁴⁺ [20]. TIFSIX-2-Cu-i atoms in the framework with different chemical properties are shown in Figure 11.

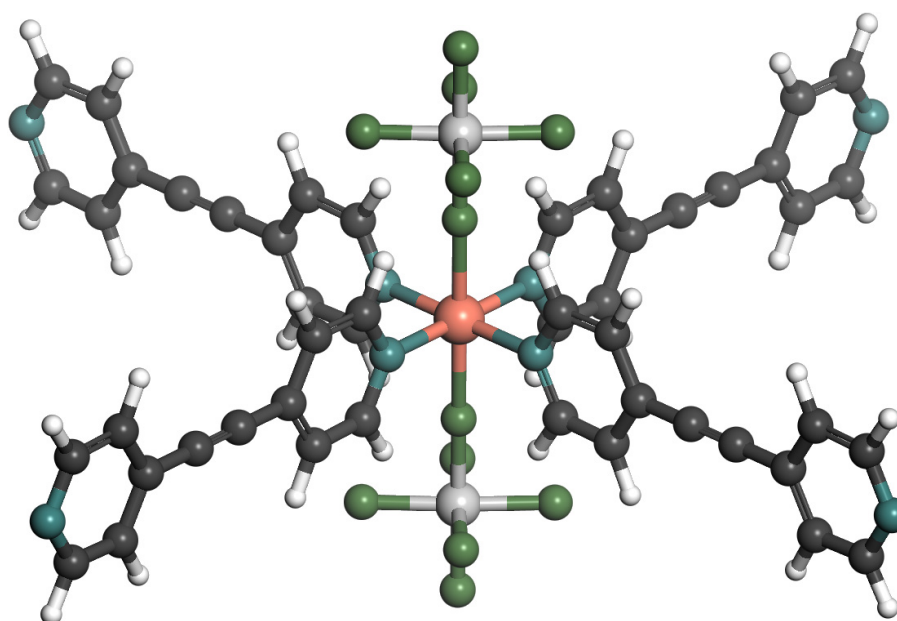


Figure 11. The chemically different atoms in TIFSIX-2-Cu-i. Atom colors: C = gray; H = white; N = blue; F = green; Ti = silver; Cu = red.

4.2. Density Functional Theory Calculations

The MOFs' structure was optimized using ab initio density functional theory (DFT) as implemented in the Vienna Ab Initio Simulation Package version 2.2 (VASP) [30], with the overall energy converged to within 10^{-5} eV per atom. The Perdew–Burke–Ernzerhof (PBE) function of the generalized gradient approximation (GGA) [31] was used to represent the electron exchange correlation, and a cutoff energy of 500 eV was set for the plane wave. According to the Monkhorst–Pack methodology, the Brillouin zone was sampled with a series of K-point grids ($2 \times 2 \times 4$). After geometrical optimization, we obtained the electron charge density and then used Density Derived Electrostatic and Chemical (DDEC6) [32,33] to calculate the atomic charge of the net atomic charge framework for each MOF atom (Table 3). DFT simulations were used to explore the redistribution of charge density in this system after adsorption of CHF₃ or CH₂F₂ molecules using the CP2K code [34]. The DZVP-MOLOPT-SR-GTH [35] basis set and the Goedecker–Teter–Hutter [36] pseudopotential were used, and the density generalization employed was a PBE with DFT-D3 [37] dispersion corrections.

Table 3. Partial charges, forcefield parameters, and atomic polarizabilities corresponding to the atom types in CHF₃ and CH₂F₂.

Atom Types	q (e)	σ (Å)	ϵ (K)	α (Å ³)
C_CHF ₃	0.719	3.52	55	1.2886
H_CHF ₃	0.016	2.6	25.2	0.4138
F_CHF ₃	−0.245	2.92	25	0.44475
C_CH ₂ F ₂	0.385	3.46	42	1.2886
H_CH ₂ F ₂	0.049	2.2	29	0.4138
F_CH ₂ F ₂	−0.2415	2.95	37	0.44475

4.3. Grand Canonical Monte Carlo Simulations

All GCMC simulations were performed with the RASPA [38] code to study CHF₃/CH₂F₂ adsorption properties under different conditions. A grand canonical systematic (μ VT) was used, where the system was under constant chemical potential, volume, and temperature. To eliminate periodic boundary conditions, we used supercell by $2 \times 2 \times 3$ replicas of the unit cell for the calculations. The van der Waals interactions were truncated to a radius of 12 Å, and tail corrections were used to approximate the contributions beyond this truncation. In the simulations, 1×10^6 Monte Carlo steps were used for the equilibration and 1×10^7 Monte Carlo steps were used for production runs. The adsorbate molecules and the adsorbate framework were treated as rigid structures. CHF₃ and CH₂F₂ were modeled as rigid tetrahedral molecules with five charged interaction sites. From previous simulation study, rigid body models were used to represent molecules as a collection of fixed geometric shapes that maintain a constant structure and orientation throughout the simulation. The host–guest and guest–guest interactions in the system were described by the short-range force and the electrostatic force, which are described by the Lennard-Jones and Coulomb potential functions (Equation (5)):

$$U_{inter}(r_{ij}) = 4\epsilon_{ij} \left[\left(\frac{\sigma_{ij}}{r_{ij}} \right)^{12} - \left(\frac{\sigma_{ij}}{r_{ij}} \right)^6 \right] + \frac{1}{4\pi\epsilon_0} \frac{q_i q_j}{r_{ij}} \quad (5)$$

where σ_{ij} and ϵ_{ij} are the collision diameter and potential well depth, respectively, r_{ij} is the distance between sites i and j , q_i denotes the atomic charge on site i , and ϵ_0 is the permittivity of free space. The cross-interactions with other molecules and frameworks are obtained using the Lorentz–Berthelot mixing rule (as shown in Equations (6) and (7)):

$$\sigma_{ij} = \frac{\sigma_{ii} + \sigma_{jj}}{2} \quad (6)$$

$$\varepsilon_{ij} = \sqrt{\varepsilon_{ii} \cdot \varepsilon_{jj}} \quad (7)$$

A polarizable forcefield was employed to achieve an accurate description of the adsorption behavior of CHF₃/CH₂F₂ in TIFSIX-2-Cu-i for molecular simulations. Back-polarization was neglected to achieve reasonable simulation times. To account for the implied polarization, we rescaled the Lennard-Jones [39] energy parameters according to the atomic polarizabilities. The Lennard-Jones energy parameters and charges of CHF₃ and CH₂F₂ were taken from previous studies [40,41]. The Lennard-Jones parameters of TIFSIX-2-Cu-i for N, C, and H were taken from the OPLS-AA forcefield, and the rest of the atoms were taken from the UFF–Dreiding hybrid forcefield [42]. The equations used to adjust the parameters in this study are as follows:

$$\varepsilon_i^{scaled} = \varepsilon_i \cdot \frac{(1 + \lambda) - \frac{\alpha_i}{\alpha_{max}}}{(1 + \lambda) - \frac{\alpha_i}{\alpha_{max}} \cdot \lambda} \quad (8)$$

α_i means the polarizability of atom_{*i*}, α_{max} means the max polarizability, and ε_i means the initial forcefield parameter. λ and ζ are scaling factors between 0 and 1, whose values depend on the discrepancy between the experimental data and the simulation results, used to rescale the Lennard-Jones energy parameters. The detailed methodology is described in Refs. [43,44]. In this study, by fitting the experimental data to the simulation results, λ was set to 0.2 and ζ to 0.9 for CH₂F₂, while λ was set to 0.9 and ζ to 0.01 for CHF₃. Tables 3 and 4 summarize all the forcefield parameters, atomic polarizabilities [45,46], and atomic charges.

Table 4. Forcefield parameters and the atomic polarizabilities corresponding to the atom types in the TIFSIX-2-Cu-i.

Atom Types	σ (Å)	ε (K)	α (Å ³)
N	3.25	85.5479	0.97157
C	3.5	40.258	1.2886
H	2.42	15.097	0.4138
F	3.0932	36.4834	0.44475
Cu	3.114	2.51	2.1963
Ti	2.8286	8.55473	3.2428

4.4. Molecular Dynamics Simulations Details

In this paper, RASPA code was used to perform molecular dynamics simulations of CHF₃/CH₂F₂ in TIFSIX-2-Cu-i. The polarized forcefield parameters from Tables 3 and 4 were employed. All MD simulations were employed for 1 ns with a time step of 0.5 fs in the NVT ensemble to explore the diffusion of the equimolar CHF₃/CH₂F₂ mixture in TIFSIX-2-Cu-i. The simulations were performed for 1×10^7 cycles, 2000 initialization cycles, and 20,000 equilibration cycles. We truncated the van der Waals interaction with a radius of 12.0 Å and used tail correction to approximate the contribution beyond this cutoff.

5. Conclusions

In this study, the adsorption mechanisms of CHF₃ or CH₂F₂ in the TIFSIX-2-Cu-i framework were studied by combining single-component adsorption experiments and molecular simulations. In order to ensure consistency between the experimental data and the simulation results, a polarization forcefield was introduced. TIFSIX-2-Cu-i has excellent CH₂F₂ adsorption capacity (3.79 mmol/g) and CH₂F₂/CHF₃ selectivity (3.17) at 3 bar and 308 K, making it a promising material to separate CHF₃/CH₂F₂ mixtures. Regarding the competitive adsorption of CHF₃–CH₂F₂ mixtures in TIFSIX-2-Cu-i, both the thermodynamic and kinetic selectivity of CH₂F₂ relative to CHF₃ were observed to be relatively high. According to the combined effect of adsorption and diffusion, TIFSIX-2-Cu-i exhibits markedly preferential adsorption of CH₂F₂ for CHF₃. The calculated heats of

adsorption indicate relatively strong interactions between CH_2F_2 and TIFSIX-2-Cu-i. The snapshots show that $\text{CHF}_3/\text{CH}_2\text{F}_2$ adsorption on TIFSIX-2-Cu-i involves multiple $\text{H}\cdots\text{F}$ interactions, where $\text{CHF}_3/\text{CH}_2\text{F}_2$ interacts with TiF_6^{2-} simultaneously. The typical binding sites of CH_2F_2 molecules in the TIFSIX-2-Cu-i channel are very similar to those of CHF_3 , and the F atoms in the TiF_6^{2-} of the TIFSIX-2-Cu-i framework preferentially adsorb with H atoms of the CH_2F_2 molecule. CH_2F_2 has more H atoms, and TIFSIX-2-Cu-i shows stronger affinity for CH_2F_2 than CHF_3 .

In conclusion, this study reveals the adsorption mechanism of $\text{CHF}_3\text{--CH}_2\text{F}_2$ mixtures in TIFSIX-2-Cu-i channels at the microscopic level. This research exploration provides an effective and superior strategy for the design and screening of highly selective adsorbents for the separation of $\text{CHF}_3\text{--CH}_2\text{F}_2$ mixtures.

Author Contributions: Conceptualization, Q.F. and S.W.; methodology, S.W. and X.C.; software, L.Z. (Lei Zhou); validation, S.W., H.Q. and L.Z. (Lei Zhou); formal analysis, Z.D., H.L. and B.L.; investigation, S.W.; resources, L.Z. (Lei Zhou); data curation, S.W., Z.W. and L.Z. (Lina Zhang); writing—original draft preparation, S.W.; writing—review and editing, S.W. and Q.F.; visualization, S.W.; supervision, Q.F., X.C. and H.Q.; project administration, S.W.; funding acquisition, Q.F. All authors have read and agreed to the published version of the manuscript.

Funding: This research was financially supported by the Natural Science Foundation of Shandong Province in China (ZR2020MB121).

Institutional Review Board Statement: Not applicable.

Informed Consent Statement: Not applicable.

Data Availability Statement: The data presented in this study are available upon request from the corresponding author.

Acknowledgments: The authors would like to thank all reviewers for their constructive advice.

Conflicts of Interest: Author Lei Zhou was employed by the company Shandong Dongyue Organosilicon Materials Co., Ltd. The remaining authors declare that the research was conducted in the absence of any commercial or financial relationships that could be construed as a potential conflict of interest.

References

1. Sovacool, B.K.; Griffiths, S.; Kim, J.; Bazilian, M. Climate change and industrial F-gases: A critical and systematic review of developments, sociotechnical systems and policy options for reducing synthetic greenhouse gas emissions. *Renew. Sustain. Energy Rev.* **2021**, *141*, 110759. [[CrossRef](#)]
2. Mota-Babiloni, A.; Navarro-Esbrí, J.; Barragán-Cervera, Á.; Molés, F.; Peris, B. Analysis based on EU Regulation No 517/2014 of new HFC/HFO mixtures as alternatives of high GWP refrigerants in refrigeration and HVAC systems. *Int. J. Refrig.* **2015**, *52*, 21–31. [[CrossRef](#)]
3. Mota-Babiloni, A.; Makhnatch, P.; Khodabandeh, R. Recent investigations in HFCs substitution with lower GWP synthetic alternatives: Focus on energetic performance and environmental impact. *Int. J. Refrig.* **2017**, *82*, 288–301. [[CrossRef](#)]
4. Velders, G.J.M.; Andersen, S.O.; Daniel, J.S.; Fahey, D.W.; McFarland, M. The importance of the Montreal Protocol in protecting climate. *Proc. Natl. Acad. Sci. USA* **2007**, *104*, 4814–4819. [[CrossRef](#)]
5. Heath, E.A. Amendment to the Montreal Protocol on Substances that Deplete the Ozone Layer (Kigali Amendment). *Int. Leg. Mater.* **2017**, *56*, 193–205. [[CrossRef](#)]
6. Benhadid-Dib, S.; Benzaoui, A. Refrigerants and their Environmental Impact Substitution of Hydro Chlorofluorocarbon HCFC and HFC Hydro Fluorocarbon. Search for an Adequate Refrigerant. *Energy Procedia* **2012**, *18*, 807–816. [[CrossRef](#)]
7. Heredia-Aricapa, Y.; Belman-Flores, J.; Mota-Babiloni, A.; Serrano-Arellano, J.; García-Pabón, J.J. Overview of low GWP mixtures for the replacement of HFC refrigerants: R134a, R404A and R410A. *Int. J. Refrig.* **2020**, *111*, 113–123. [[CrossRef](#)]
8. Hu, J.; Liu, C.; Liu, L.; Li, Q. Thermal energy storage of R1234yf, R1234ze, R134a and R32/MOF-74 nanofluids: A molecular simulation study. *Materials* **2018**, *11*, 1164. [[CrossRef](#)]
9. Hu, G.; Wang, Z.; Zhang, W.; He, H.; Zhang, Y.; Deng, X.; Li, W. MIL-161 Metal–Organic Framework for Efficient Au(III) Recovery from Secondary Resources: Performance, Mechanism, and DFT Calculations. *Molecules* **2023**, *28*, 5459. [[CrossRef](#)]
10. Apriliyanto, Y.B.; Faginas-Lago, N.; Evangelisti, S.; Bartolomei, M.; Leininger, T.; Pirani, F.; Pacifici, L.; Lombardi, A. Multilayer Graphitryne Membranes for Separation and Storage of CO_2 : Molecular Dynamics Simulations of Post-Combustion Model Mixtures. *Molecules* **2022**, *27*, 5958. [[CrossRef](#)]
11. Tagliabue, M.; Farrusseng, D.; Valencia, S.; Aguado, S.; Ravon, U.; Rizzo, C.; Corma, A.; Mirodatos, C. Natural gas treating by selective adsorption: Material science and chemical engineering interplay. *Chem. Eng. J.* **2009**, *155*, 553–566. [[CrossRef](#)]

12. Wang, Q.; Yu, Y.; Li, Y.; Min, X.; Zhang, J.; Sun, T. Methane separation and capture from nitrogen rich gases by selective adsorption in microporous materials: A review. *Sep. Purif. Technol.* **2022**, *283*, 120206. [[CrossRef](#)]
13. Yancey, A.D.; Terian, S.J.; Shaw, B.J.; Bish, T.M.; Corbin, D.R.; Shiflett, M.B. A review of fluorocarbon sorption on porous materials. *Microporous Mesoporous Mater.* **2022**, *331*, 111654. [[CrossRef](#)]
14. Peng, J.; Fu, C.; Zhong, J.; Ye, B.; Xiao, J.; Duan, C.; Lv, D. Efficient Selective Capture of Carbon Dioxide from Nitrogen and Methane Using a Metal-Organic Framework-Based Nanotrap. *Molecules* **2023**, *28*, 7908. [[CrossRef](#)]
15. Li, Y.; Bai, Y.; Wang, Z.; Gong, Q.; Li, M.; Bo, Y.; Xu, H.; Jiang, G.; Chi, K. Exquisitely Constructing a Robust MOF with Dual Pore Sizes for Efficient CO₂ Capture. *Molecules* **2023**, *28*, 6276. [[CrossRef](#)] [[PubMed](#)]
16. Xu, F.; Wu, Y.; Wu, J.; Lv, D.; Yan, J.; Wang, X.; Chen, X.; Liu, Z.; Peng, J. A Microporous Zn(bdc)(ted)_{0.5} with Super High Ethane Uptake for Efficient Selective Adsorption and Separation of Light Hydrocarbons. *Molecules* **2023**, *28*, 6000. [[CrossRef](#)] [[PubMed](#)]
17. Ghazvini, M.F.; Vahedi, M.; Nobar, S.N.; Sabouri, F. Investigation of the MOF adsorbents and the gas adsorptive separation mechanisms. *J. Environ. Chem. Eng.* **2021**, *9*, 104790. [[CrossRef](#)]
18. Wu, D.; Zhang, P.-F.; Yang, G.-P.; Hou, L.; Zhang, W.-Y.; Han, Y.-F.; Liu, P.; Wang, Y.-Y. Supramolecular control of MOF pore properties for the tailored guest adsorption/separation applications. *Coord. Chem. Rev.* **2021**, *434*, 213709. [[CrossRef](#)]
19. Wanigarathna, D.K.; Gao, J.; Liu, B. Metal organic frameworks for adsorption-based separation of fluorocompounds: A review. *Mater. Adv.* **2020**, *1*, 310–320. [[CrossRef](#)]
20. Jiang, M.; Cui, X.; Yang, L.; Yang, Q.; Zhang, Z.; Yang, Y.; Xing, H. A thermostable anion-pillared metal-organic framework for C₂H₂/C₂H₄ and C₂H₂/CO₂ separations. *Chem. Eng. J.* **2018**, *352*, 803–810. [[CrossRef](#)]
21. Yu, Y.; Yang, L.; Tan, B.; Hu, J.; Wang, Q.; Cui, X.; Xing, H. Remarkable separation of C₅ olefins in anion-pillared hybrid porous materials. *Nano Res.* **2020**, *14*, 541–545. [[CrossRef](#)]
22. Li, B.; Chen, B. Fine-Tuning Porous Metal-Organic Frameworks for Gas Separations at Will. *Chem* **2016**, *1*, 669–671. [[CrossRef](#)]
23. Bajpai, A.; O’Nolan, D.; Madden, D.G.; Chen, K.-J.; Pham, T.; Kumar, A.; Lusi, M.; Perry, J.J.; Space, B.; Zaworotko, M.J. The effect of centred versus offset interpenetration on C₂H₂ sorption in hybrid ultramicroporous materials. *Chem. Commun.* **2017**, *53*, 11592–11595. [[CrossRef](#)]
24. Zhang, Q.; Chen, X.; Fu, Q.; Qin, H.; Zhang, H.; Li, H.; Wang, S.; Dong, Z.; Zhang, Z.; Wang, M. Study on the Adsorption Separation of CHF₃/N₂ by an SIFSIX-3-Ni Metal–Organic Framework. *Ind. Eng. Chem. Res.* **2023**, *62*, 13627–13636. [[CrossRef](#)]
25. Kołaczkiwicz, J.; Bauer, E. Clausius-Clapeyron equation analysis of two-dimensional vaporization. *Surf. Sci.* **1985**, *155*, 700–714. [[CrossRef](#)]
26. Chen, K.-J.; Scott, H.S.; Madden, D.G.; Pham, T.; Kumar, A.; Bajpai, A.; Lusi, M.; Forrest, K.A.; Space, B.; Perry, J.J.; et al. Benchmark C₂H₂/CO₂ and CO₂/C₂H₂ Separation by Two Closely Related Hybrid Ultramicroporous Materials. *Chem* **2016**, *1*, 753–765. [[CrossRef](#)]
27. Bokii, G. *Kristalokhimiya, Izd; Nauka: Moskva, Russia*, 1971.
28. Zhou, L.; Zhou, Y.; Li, M.; Chen, P.; Wang, Y. Experimental and Modeling Study of the Adsorption of Supercritical Methane on a High Surface Activated Carbon. *Langmuir* **2000**, *16*, 5955–5959. [[CrossRef](#)]
29. Nugent, P.; Rhodus, V.; Pham, T.; Tudor, B.; Forrest, K.; Wojtas, L.; Space, B.; Zaworotko, M. Enhancement of CO₂ selectivity in a pillared pcu MOM platform through pillar substitution. *Chem. Commun.* **2013**, *49*, 1606–1608. [[CrossRef](#)]
30. Kresse, G.; Furthmüller, J. Efficient iterative schemes for ab initio total-energy calculations using a plane-wave basis set. *Phys. Rev. B* **1996**, *54*, 11169. [[CrossRef](#)]
31. Perdew, J.P.; Burke, K.; Ernzerhof, M. Generalized Gradient Approximation Made Simple. *Phys. Rev. Lett.* **1996**, *77*, 3865–3868. [[CrossRef](#)]
32. Limas, N.G.; Manz, T.A. Introducing DDEC6 atomic population analysis: Part 2. Computed results for a wide range of periodic and nonperiodic materials. *RSC Adv.* **2016**, *6*, 45727–45747. [[CrossRef](#)]
33. Limas, N.G.; Manz, T.A. Introducing DDEC6 atomic population analysis: Part 4. Efficient parallel computation of net atomic charges, atomic spin moments, bond orders, and more. *RSC Adv.* **2018**, *8*, 2678–2707. [[CrossRef](#)] [[PubMed](#)]
34. Hutter, J.; Iannuzzi, M.; Schiffmann, F.; VandeVondele, J. cp2k: Atomistic simulations of condensed matter systems. *Wiley Interdiscip. Rev. Comput. Mol. Sci.* **2014**, *4*, 15–25. [[CrossRef](#)]
35. VandeVondele, J.; Hutter, J. Gaussian basis sets for accurate calculations on molecular systems in gas and condensed phases. *J. Chem. Phys.* **2007**, *127*, 114105. [[CrossRef](#)] [[PubMed](#)]
36. Goedecker, S.; Teter, M.; Hutter, J. Separable dual-space Gaussian pseudopotentials. *Phys. Rev. B* **1996**, *54*, 1703. [[CrossRef](#)] [[PubMed](#)]
37. Grimme, S.; Antony, J.; Ehrlich, S.; Krieg, H. A consistent and accurate ab initio parametrization of density functional dispersion correction (DFT-D) for the 94 elements H-Pu. *J. Chem. Phys.* **2010**, *132*, 154104. [[CrossRef](#)] [[PubMed](#)]
38. Dubbeldam, D.; Calero, S.; Ellis, D.E.; Snurr, R.Q. RASPA: Molecular simulation software for adsorption and diffusion in flexible nanoporous materials. *Mol. Simul.* **2016**, *42*, 81–101. [[CrossRef](#)]
39. Schnabel, T.; Vrabec, J.; Hasse, H. Unlike Lennard–Jones parameters for vapor–liquid equilibria. *J. Mol. Liq.* **2007**, *135*, 170–178. [[CrossRef](#)]
40. Fu, Q.; Tanaka, H.; Miyahara, M.T.; Qin, Y.; Shen, Y.; Zhang, D. CHF₃–CHClF₂ Binary Competitive Adsorption Equilibria in Graphitic Slit Pores: Monte Carlo Simulations and Breakthrough Curve Experiments. *Ind. Eng. Chem. Res.* **2018**, *57*, 6440–6450. [[CrossRef](#)]
41. Yang, T.; Siepmann, J.I.; Wu, J. Phase Equilibria of Difluoromethane (R32), 1,1,1,2-Tetrafluoroethane (R134a), and trans-1,3,3,3-Tetrafluoro-1-propene (R1234ze(E)) Probed by Experimental Measurements and Monte Carlo Simulations. *Ind. Eng. Chem. Res.* **2020**, *60*, 739–752. [[CrossRef](#)]

42. Rappe, A.K.; Casewit, C.J.; Colwell, K.S.; Goddard, W.A., III; Skiff, W.M. UFF, a full periodic table force field for molecular mechanics and molecular dynamics simulations. *J. Am. Chem. Soc.* **1992**, *114*, 10024–10035. [[CrossRef](#)]
43. Becker, T.M.; Dubbeldam, D.; Lin, L.-C.; Vlugt, T.J.H. Investigating polarization effects of CO₂ adsorption in MgMOF-74. *J. Comput. Sci.* **2016**, *15*, 86–94. [[CrossRef](#)]
44. Becker, T.M.; Heinen, J.; Dubbeldam, D.; Lin, L.-C.; Vlugt, T.J.H. Polarizable Force Fields for CO₂ and CH₄ Adsorption in M-MOF-74. *J. Phys. Chem. C* **2017**, *121*, 4659–4673. [[CrossRef](#)] [[PubMed](#)]
45. Shannon, R.D. Dielectric polarizabilities of ions in oxides and fluorides. *J. Appl. Phys.* **1993**, *73*, 348–366. [[CrossRef](#)]
46. Van Duijnen, P.T.; Swart, M. Molecular and atomic polarizabilities: Thole's model revisited. *J. Phys. Chem. A* **1998**, *102*, 2399–2407. [[CrossRef](#)]

Disclaimer/Publisher's Note: The statements, opinions and data contained in all publications are solely those of the individual author(s) and contributor(s) and not of MDPI and/or the editor(s). MDPI and/or the editor(s) disclaim responsibility for any injury to people or property resulting from any ideas, methods, instructions or products referred to in the content.